High-performance electrochemical biosensor for nonenzymatic H_2O_2 sensing based on Au@C-Co_3O_4 heterostructures

Hongxia Dai, Yonglei Chen, Xiaoying Niu, Congjie Pan, HongLi Chen, Xingguo Chen

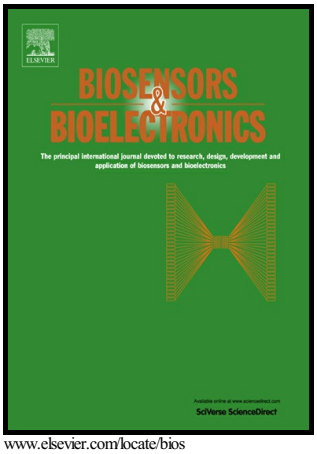

www.elsevier.com/locate/bios

PII: S0956-5663(18)30523-2
DOI: https://doi.org/10.1016/j.bios.2018.07.022
Reference: BIOS10611

To appear in: *Biosensors and Bioelectronic*

Received date: 28 April 2018
Revised date: 8 July 2018
Accepted date: 10 July 2018

Cite this article as: Hongxia Dai, Yonglei Chen, Xiaoying Niu, Congjie Pan, HongLi Chen and Xingguo Chen, High-performance electrochemical biosensor for nonenzymatic H_2O_2 sensing based on Au@C-Co_3O_4 heterostructures, *Biosensors and Bioelectronic,* https://doi.org/10.1016/j.bios.2018.07.022

High-performance electrochemical biosensor for nonenzymatic H_2O_2 sensing based on Au@C-Co_3O_4 heterostructures

Hongxia Dai[a,b,d], Yonglei Chen[a,b*], Xiaoying Niu[a,b], Congjie Pan[a,b], HongLi Chen[a,b], Xingguo Chen[a,bc*]

[a]State Key Laboratory of Applied Organic Chemistry, Lanzhou University, Lanzhou 730000, China

[b]Department of Chemistry, Lanzhou University, Lanzhou 730000, China

[c]Key Laboratory of Nonferrous Metal Chemistry and Resources Utilization of Gansu Province, Lanzhou 730000, China

[d]Gansu University of Chinese Medicine, Lanzhou 730000, China

chyl@lzu.edu.cn

chenxg@lzu.edu.cn

[*]Corresponding authors. Tel.: 86-931-8912763; fax: 86-931-8912582

Abstract

An ingenious and viable method for preparing heterogeneous Co_3O_4 dodecahedrons that contain carbon and encapsulated Au nanoparticles (Au@C-Co_3O_4) was proposed via pyrolysis of Au

nanoparticle-encapsulated zeolitic imidazolate framework-67 (Au@ZIF-67). The obtained Au@C-Co_3O_4 possessed hierarchically porous structure, abundant active sites, excellent conductivity, and durability, all of which can significantly improve the analysis performance of the biosensor. Meanwhile, the fabricated electrode based on the porous Au@C-Co_3O_4 showed remarkable electrocatalytic performance towards H_2O_2 with a limit of detection of 19 nM and ultra-high sensitivity of 7553 μA mM^{-1} cm^{-2}, even when the Au content in the composite was as low as 0.85 wt%. This novel biosensor was successfully used to monitor H_2O_2 concentration released from living cells, and the results can be used to identify cancer cells, thus advancing the use of transition metal oxides in the field of biosensing.

Keywords**:** Co_3O_4, Au nanoparticles, Nonenzymatic biosensor, Hydrogen peroxide, Living cells.

1. Introduction

Rapid, accurate, and reliable determination of hydrogen peroxide (H_2O_2) is of great importance in pharmaceutical, clinical, industrial, and environmental analyses (Belousov et al., 2006; Yoo et al., 2011). In

biological systems, H_2O_2 is a reactive oxygen and can react with various cellular targets in a concentration-dependent manner (Halliwell et al., 2000). At moderate concentration, H_2O_2 (0.001~0.7 μM) functions as a signaling molecule, controlling different essential processes in plants and mammals, and excess H_2O_2 is implicated in arteriosclerosis, cancer, stroke, diabetes, and a host of other serious diseases (Miller et al., 2010). Therefore, real-time detection of H_2O_2 *in vivo* plays an important role in the diagnosis and treatment of diseases.

Among various analytical techniques for H_2O_2, enzyme-based electrochemical sensors are very attractive because of their high sensitivity and good selectivity (Dai et al., 2017; Liu et al., 2017). However, they still suffer from some drawbacks, such as the high cost of enzymes, the complexity and tediousness of the enzyme immobilization process, and instability because of the inherent fragility of enzymes. Thus, with the use of versatile materials, including noble metals (e.g., Au, Pt, and PtAu), transition metal oxides (e.g., Fe_3O_4, Co_3O_4, TiO_2, and CuO), nonmetal catalysts (e.g., graphitic carbon nitrides, N-doped graphitic carbons), and nanocomposites, nonenzymatic H_2O_2 sensors based on direct electrocatalytic oxidation or reduction are expected to replace enzyme-based sensors (Bai et al., 2016; Chakraborty et al., 2009; Liu et al., 2017; Sun et al., 2013; Sun et al., 2017; Wang et al., 2010; Wang et al., 2014). Among these materials, cobalt oxide (Co_3O_4), which is a kind of

intrinsic *p*-type transition metal oxide, is greatly appealing because of its unique properties such as low cost, high electrochemical stability and environmental friendliness (Kumar et al., 2016; Bajdich et al., 2013). However, these Co_3O_4-based sensors often had poor electronic conductivity or close-packed structures, which reduce their specific surface area and greatly weaken their electrochemical performance (Jiang et al., 2012). In this respect, the rational design of composite materials by combining highly electrocatalytic materials with a conductive substance is an effective way to achieve good electrochemical performance (Cheng et al., 2018; Zhang et al., 2015). Specifically, noble metal nanoparticles (e.g., Au and Pt) are the best choice for composite materials because of their excellent conductivity and catalytic activity (Bai et al., 2017). Nevertheless, the current detection results are not as good as required to be, and this has been attributed to two major reasons: (1) it is extremely challenging to highly integrate noble metal nanoparticles into metal oxides because different materials that have distinct physical and chemical properties are not well incorporated simultaneously in the synthesis process (Zhang et al., 2013), and (2) the inevitable aggregation phenomenon of metal nanoparticles reduces their surface energy, which greatly hampers reusability and thus limits their practical application (Hu et al., 2015). To circumvent these issues, there is an urgently need to develop alternative Co_3O_4-based materials for detecting H_2O_2 with high

sensitivity and strong long-term stability under physiological conditions.

Recently, a class of highly porous materials known as metal organic frameworks (MOFs) has attracted significant attention (Wu et al., 2015; Yu et al., 2015). Owing to the ability to mutually control their porous properties, chemical composition, and functionalities, MOFs have been used as unique host matrices for various functional species and excellent sacrificial templates to develop new types of composite materials with improved catalytic, optical and electrically conductive properties (Liu et al., 2015; Lu et al., 2012). This inspired us to use Au nanoparticle-functionalized MOFs to design an appropriate template to produce Co_3O_4-based materials with improved performance by a subsequent pyrolysis process. Zeolitic imidazolate framework-67 (ZIF-67), which is a highly porous Co-MOF, is commonly used as a sacrificial template because it can be synthesized at room temperature and converted into a highly graphitic carbon structure and catalytic cobalt oxide moieties (Aijaz et al., 2016).

Herein, we developed an ingenious method using pyrolysis of Au nanoparticle--functionalized ZIF-67 (Au@ZIF-67) to fabricate porous dodecahedrons (Au@C-Co_3O_4) that contain interconnected Au nanoparticles (Au NPs), carbon, and Co_3O_4. To take full advantage of MOFs in composition regulation, the as-prepared Au@C-Co_3O_4 forms a porous structure with a high specific surface area, and can be easily

manipulated and attached to an electrode surface without the help of an entrapment matrix. Heterogeneous Au@C-Co_3O_4 was used as a highly active catalyst for electrochemical detection of H_2O_2 with nM detection sensitivity, which is suitable for monitoring and quantifying the H_2O_2 released from cells. The strategy introduced in the present work offers new prospects for the rational design and synthesis of MOF-derived materials with unprecedented electrocatalytic activities and stabilities, which will have broad impact on sensor development.

2. Experimental

2.1 Materials

$HAuCl_4$ (99.99%), H_2PtCl_6 (99.99%), $Co(NO_3)_2 \cdot 6H_2O$ (99.999%), 2-methylimidazole (>90%), polyvinylpyrrolidone (PVP), 3-(4,5-dimethyl -2-thiazolyl)-2,5-diphenyl-2H-tetrazolium bromide (MTT) and catalase (E.C. 1.11.1.6, from bovine liver, 3000 U mg^{-1}) were purchased from Sigma-Aldrich (St. Louis, MO, USA). Phorbol 12-myristate 13-acetate (PMA) was purchased from Wako Pure Chemical Industries (Osaka, Japan). Human renal tubular epithelial cells (HKC), human cervical cancer cells (HeLa) and human breast cancer cells (MCF-7) were obtained from Gansu University of Chinese Medicine (Lanzhou, China). Amplex Red Hydrogen Peroxide Assay kit was purchased from Thermo

Fisher (Shanghai, China). All chemical reagents were of analytical grade and utilized without further purification. Doubly distilled water (resistance >18 MΩ cm^{-1}, Milli-Q purification system, Bedford, MA, USA) was employed throughout all experiments.

2.2 Characterization

The morphologies and surface structures were characterized with field-emission scanning electron microscope (SEM, ZEISS, Germany) and transmission electron microscopy (TEM, JEOL, Japan). The samples were suspended in methanol and drop-cast onto a carbon-coated 200-mesh copper grid, and subsequently dried at room temperature. Selected area electron diffraction (SAED) patterns were obtained by positioning the selected area diffraction aperture of the TEM over the desired area of the substrate. The elemental composition was analyzed with an energy-dispersive spectrometer (EDS) (JSM-5900LV). Powder X-ray diffraction (PXRD) analysis was performed on a Bruker D8 Advance Diffractometer (Germany). X-ray photoelectron spectroscopy analysis (XPS) was carried out with ESCALAB Mark II (VG Scientific, UK). The binding energy is calibrated with the C 1s position of contaminant carbon in the vacuum chamber of the XPS instrument (284.8 eV). The N_2 sorption-desorption isotherms were performed on an ASAP 2020 instrument (Micromeritics, USA). The Brunauer-Emmett-Teller

(BET) method was used to calculate the specific surface area. Thermogravimetric analysis (TGA) was taken with a thermogravimetric analyzer (Perkin-Elmer TGA-7, USA). The content of Au in Au@ZIF-67 or Au@C-Co_3O_4 was determined using an inductively coupled plasma atomic emission spectrometer (ICP-AES, TJA IRIS Advantage ER/S, USA). Raman spectra were measured using Raman spectroscopy system (Photon Design, Horiba-Jobin-Yvon T64000).

2.3 Synthesis of porous Au@C-Co_3O_4

Au NPs (~13 nm) were synthesized using an established method and their surfaces were functionalized with polyvinylpyrrolidone (PVP) during synthesis (Frens et al., 1973). PVP-stabilized Au NPs were filtered through a 200 nm membrane to remove large aggregates and then dispersed in methanol with an absorbance value of ~1.0 at 520 nm. Porous Au@C-Co_3O_4 dodecahedrons were prepared via two-steps: fabrication of Au@ZIF-67 and subsequent pyrolysis. First, 1.5 mL Au NP solution of desired concentration was mixed with 15 mL of $Co(NO_3)_2 \cdot 6H_2O$ solution (0.125 mM) and 15 mL of 2-methyl imidazole solution (0.500 mM). This mixture was then allowed to react via sonication for 5 min to produce sub-micron Au@ZIF-67 with great stability. The resulting fuchsia solid (Au@ZIF-67) was collected via centrifugation, washed three times with methanol, and vacuum-dried

overnight. Next, the as-prepared Au@ZIF-67 was directly carbonized at 350 °C for 4 h in a temperature-programmed furnace under a N_2 atmosphere followed by mild oxidative calcination at 250 °C for 2 h. After cooling to room temperature, the fuchsia Au@ZIF-67 was finally converted into black powder, and the resulting product was denoted as Au@C-Co_3O_4. For comparison, the carbon-containing cobalt oxide (C-Co_3O_4) was prepared using the same procedure but without the addition of Au NPs.

2.4 Fabrication of Au@C-Co_3O_4 modified electrode

The glassy carbon electrode (GCE, 3 mm diameter) was polished to a mirror-like surface using 0.3 and 0.05 μm alumina slurries. The GCE was then thoroughly rinsed sequentially with deionized water and anhydrous ethanol. Au@C-Co_3O_4 aqueous solution (8 μL, 1.0 mg mL^{-1}) was drop-cast onto a cleaned GCE and dried in air to obtain Au@C-Co_3O_4/GCE. For comparison, C-Co_3O_4 and Au NPs were also used to prepare modified electrodes in a similar way as described above, and these electrodes were denoted as C-Co_3O_4/GCE and Au/GCE, respectively.

2.5 Electrochemical measurements

All electrochemical measurements were performed on a CHI660D

electrochemical workstation (Chenhua Instruments Company, Shanghai, China). A conventional three-electrode cell was used with modified glass carbon electrode as the working electrode, Ag/AgCl (in saturated KCl solution) as the reference electrode, and platinum wire as the counter electrode, respectively. All potential in this paper were referred to Ag/AgCl. Electrochemical impedance spectroscopy (EIS) measurements were carried out in 5.0 mM $K_3Fe(CN)_6/K_4Fe(CN)_6$ (1:1) containing 0.1 M KCl, while the applied perturbation amplitude was 0.005 V, the frequencies swept from 10^5 to 10^{-2} Hz. Amperometric experiments were performed in a constantly stirred cell with the successive addition of H_2O_2 into 10.0 mL of 0.1 M PBS supporting electrolyte (pH 7.4) at 25 °C. The electrode potential was set at +0.50 V vs Ag/AgCl.

2.6 Detection of H_2O_2 Released from Living Cells

Human renal tubular epithelial cells (HKC), human cervical cancer cells (HeLa) and human breast cancer cells (MCF-7) were cultured in Dulbecco's modified Eagle medium containing 10% (v/v) fetal bovine serum, 100 U mL^{-1} penicillin, and 100 mg mL^{-1} streptomycin at 37 °C in a 5% CO_2 environment. After growing to 90% confluence, the cells were collected by centrifugation and washed three times with PBS (10 mM, pH 7.4). Cell number was estimated by a hemocytometer. During the test, a pellet that each contained ca. 1×10^6 cells was resuspended into 10.0 mL

of PBS (0.1 M, pH 7.4). The cell samples containing catalase (50 μL, 300 U mL^{-1}) were used as the control. For electrochemical measurements, 10 μL of Phorbol 12-myristate 13-acetate (PMA, 1 μg mL^{-1}) was injected into the tested system and the amperometric current responses at the applied potential of 0.50 V were recorded as shown in Scheme 1.

3. Results and discussion

3.1 Characterization of porous Au@C-Co_3O_4

Porous dodecahedrons were prepared via the two-step route shown in **Scheme 1**. First, PVP-stabilized Au NPs that had a diameter of ~13 nm (Fig. S1) were successively adsorbed onto the surfaces of the growing ZIF-67 crystals to form Au@ZIF-67 using ultrasonic-assisted treatment. The size and morphology of the as-synthesized Au@ZIF-67 was investigated by FESEM. As clearly seen in Fig. 1A, Au@ZIF-67 consisted of isolated ~450 nm wide crystals of rhombic dodecahedral shapes together with intergrown crystals. Each crystal contained multiple Au NPs that were fully encapsulated by ZIF-67 and were well dispersed (Fig. 1A, insert I). Ultrasound irradiation induced enhanced mass transport due to acoustic streaming and turbulent mixing, and this generated high-velocity interparticle collision in the bulk solution to

overcome van der Waals forces; this effectively restricted the aggregation of Au-NPs (Muthoosamy et al., 2017). The Au content in Au@ZIF-67 was determined to be 0.38 wt% using ICP analysis. A successive two-step thermal conversion process was then introduced to transform Au@ZIF-67 composites into porous Au@C-Co_3O_4 dodecahedrons. Thermogravimetric analysis (TGA) (Fig. S2) showed that the Au@ZIF-67 composites are stable in N_2 up to 400 °C without obvious weight loss. Thermal treatment in N_2 is favorable for preserving the configuration of ZIF-67because carbon generated at the first calcination might act as a temporal buffer, effectively hindering further contraction of MOFs (Xu et al., 2012). On the basis of TGA results, the as-synthesized Au@ZIF-67 template was first heated at 350 °C in N_2 and then annealed at 250 °C in aflow of air to obtain the final products.

After calcination, a fluffy black powder was obtained, which preserved well the uniform size and dodecahedral shape of Au@ZIF-67 precursors (Fig. 1B). However, the surface of the particles became much rougher and a few slitlike pores were visible on the edge of the polyhedral particles, because of the decomposition and contraction when being heated. A TEM image showed that these particles were well integrated with the Au NPs (Fig. 1B, insert II). Notably, the Au NPs in the material were still well dispersed, and there was no apparent agglomeration, which is crucial for improving electrochemical performance. Also, the

corresponding EDS (Fig. 1C) and ICP analysis explicitly confirm the existence of Au NPs in the composites. The Au content was as low as 0.85 wt%, which is beneficial for reducing manufacturing costs. Selected area electron diffraction demonstrated that the obtained product had polycrystalline structure (Fig. 1C, insert III). The crystalline nature of the resulting material was further investigated by PXRD. As shown in Fig. 1D, all of the diffraction peaks of the formed Au@ZIF-67 in the 2θ range of 5–60^{o} match well with published results of the typical crystalline structure of ZIF-67 (Yang et al., 2015), and this suggests that incorporating of nanoparticles does not obviously degrade the crystallinity of the framework matrices. After calcination, all of the diffraction peaks of the product correspond well to pure cubic spinel Co_3O_4 (JCPDS 42-1467). The diffraction peaks at 2θ values of 18.9°, 31.2°, 36.8°, 38.6°, 44.8°, 55.6°, and 59.3° correspond to (111), (220), (311), (222), (400), (440), and (511) crystal planes, respectively (Kong et al., 2014). Note that the diffraction peaks that can be assigned to Au NPs were too weak to be observed clearly in the patterns of the hybrid composites, and this was presumably because of their low contents and small sizes (Shi et al., 2013).

XPS results further indicate that the calcined product contains Co, C, O, and Au elements without other impurities (Fig. 2A), which is consistent with the results of EDS analysis. The best deconvoluted Co 2p

spectrum exhibits two characteristic broad peaks centered at 780.6 and 796.1 eV, corresponding to the Co 2p 3/2 and Co 2p 1/2 spin−orbit peaks of the Co_3O_4 phase, respectively (Fig. 2B). The two fitted peaks at 530.5 and 532.0 eV in the O 1s spectrum are associated with O^{2-} ions in oxygen-deficient regions within the Co_3O_4 matrix (Fig. 2C). C 1s analysis indicates that two different types of carbon atoms: sp^2-hybridized graphite-like carbon (C=C) at 284.6 eV and sp^3-hybridized diamond-like carbon (C-C) at 285.5 eV (Fig. 2D). In the Au 4f spectrum, there are two distinct peaks at 84.5 and 88.3 eV, which indicate that most of the gold particles were present in the metallic state (Fig. 2E). The formation of graphitic carbon has been further confirmed by Raman spectroscopy (Fig. S3). Well-graphitized carbon interacted closely with entrapped Co_3O_4 and Au species (Fig. S4), and this led to interfacial electron transfer. To prove this, alternating current impedance was used to explore the interfacialproperties of surface modified electrodes. Charge transfer resistance (R_{ct}) controls the electron transfer kinetics of the $Fe(CN)_6^{3-/4-}$ redox probe at the electrode interface. An equivalent circuit was used to fit the impedance curve (insert of Fig. 2F). In the equivalent circuit, R_1, W_1 and CPE are the resistance of the solution, the Warburg impedance and constant phase elements, respectively. As seen in Fig. 2F, the high R_{ct} (3040 ohm) of C-Co_3O_4/GCE indicates that there is an inefficient electron transfer process atthe surface, whereas the lower R_{ct} (227 ohm) of

Au/GCE, which uses the highly conductive Au NPs. When Au nanoparticles were doped into C-Co_3O_4, the R_{ct} of Au@C-Co_3O_4/GCE (987 ohm) was clearly lower than that of C-Co_3O_4/GCE, and this confirms the enhanced conductivity of Au@C-Co_3O_4.

Moreover, N_2 adsorption measurement of Au@C-Co_3O_4 (Fig. S5) showed a type I isotherm with an H3-type hysteresis loop and a Brunauer-Emmett-Teller (BET) specific surface area of 777 m^2 g^{-1}, which was much higher than that previously reported for Co_3O_4 particles (up to ~251 m^2 g^{-1}). This result was an exact manipulation of the calcination conditions of Au@ZIF-67 (Liu et al., 2014; Ma et al., 2014). The average pore sizes of Au@C-Co_3O_4 was concentrated at ~0.77 nm and ~1.22 nm, and the total volume of the pores was 0.54 cm^3 g^{-1}. A hierarchically porous structure with large surface area can provide more active sites for redox reaction, which thus causes Au@C-Co_3O_4 to have excellent electrochemical properties.

3.2 Electrocatalytic Activities of Au@C-Co_3O_4 toward H_2O_2

Figs. 3A and 3B show the respective cyclic voltammograms (CVs) for Au NPs, C-Co_3O_4, and Au@C-Co_3O_4 with and without 0.05 mM H_2O_2. In 0.1 M NaOH or in 0.1 M PBS (pH 7.4), all of the Co_3O_4-based materials exhibited two pairs of redox peaks and had higher oxidation peak currents compared to that of pure Au NPs. The hollow dodecahedral

Au@C-Co_3O_4 was the most active catalyst. The two pairs of well-defined peaks (I/II and III/IV) can be attributed to the reversible conversion between the Co_3O_4/CoOOH and CoOOH/CoO_2 redox couples, respectively (Zhang et al., 2016):

$$Co_3O_4 + OH^- + H_2O \rightleftharpoons 3CoOOH + e^- \quad (1)$$

$$CoOOH + OH^- \rightleftharpoons CoO_2 + H_2O + e^- \quad (2)$$

Interestingly, the maximum CV response to 0.05 mM H_2O_2 was obtained with Au@C-Co_3O_4/GCE in 0.1 M PBS (Fig. S6). The high activity of Au@C-Co_3O_4 may be caused by the unique anisotropic architectures and the synergistic catalytic effect of Co_3O_4, Au NPs and amorphous carbon. Because many biological samples need to be tested under physiological conditions in practical applications, 0.1 M PBS (pH 7.4) was chosen as the electrolyte for subsequent experiments. Fig. 3C showed that the CV curves had good symmetry at different potential scan rates, and this indicated the stable reversibility of the redox reaction of Co_3O_4 particles. Moreover, it can be seen that both anodic and cathodic peak currents increase linearly with an increase in the scan rate, suggesting a surface-controlled electrochemical process. It is generally known that H_2O_2 is an active molecule and tends to decompose slowly. Addition of Co_3O_4 can accelerate decomposition of H_2O_2, especially in neutral or alkaline conditions. Because the redox potential of H_2O_2/O_2 is very low at a high pH, H_2O_2 is more easily oxidized by Co^{3+}. Thus, the anodic peak

currents increased with an increase in H_2O_2 concentration accompanied by a decrease in cathodic current (Fig. 3D). According to previous reports, electrocatalytic oxidation of H_2O_2 by Au@C-Co_3O_4 should involve the following reaction (Heli et al., 2014):

$$2Co(III)+H_2O_2+2OH^- \rightarrow 2Co(II)+ 2H_2O+ O_2 \qquad (3)$$

With conversion from Co(III) to Co(II), the forward reaction (Co(II)→ Co(III)) is greatly favored, and this results in enhanced oxidation current at +0.50 V upon the addition of H_2O_2.

The applied potential for amperometric determinations of H_2O_2 was optimized to obtain the best electrochemical response (Fig. S7). The best catalytic current response for H_2O_2 was obtained only at +0.50 V on Au@C-Co_3O_4/GCE. Fig. 3E shows the typical amperometric response at Au@C-Co_3O_4/GCE upon successive additions of H_2O_2. The proposed electrode responded quickly to the oxidation of H_2O_2 and achieved a steady-state current within 4 s. The calibration curve of current versus H_2O_2 concentration exhibited two different linear relationships; one was from 0.05 to 100 μM (R^2=0.9998) with a linear regression equation of I(μA)=0.528c(μM)+0.0034, and the other was from 0.1 to 3.0 mM (R^2=0.9992) with a linear regression equation of I(μA)=0.095c(μM)+41.53 (Fig. 3F). The limit of detection for H_2O_2 was estimated to be 19 nM with a signal-to-noise ratio of 3, and this

demonstrated the excellent electrochemical sensing ability. The sensitivity of the sensor was determined to be 7553 μA mM^{-1} cm^{-2}, which was much higher than those of previously reported electrochemical sensors based on Co_3O_4 composites (Table S1). The high sensitivity and low detection limit could be attributed to: (1) the hollow porous structure of Co_3O_4 with larger surface area (Figs. S8 and S9, and Table S2), which provided numerous active sites and allowed easy diffusion of H_2O_2 to the electrode (Li et al., 2016), (2) well-dispersed Au NPs and graphitic carbon, which can increase the conductivity of materials and thus enhance the sensitivity of the H_2O_2 detection, and (3) Co_3O_4, Au NPs and graphitic C having the ability to catalyze H_2O_2 oxidation when they were integrated. The newly formed Au@C-Co_3O_4 exhibited stronger catalytic performance (Fig. S10). Hence, Au@C-Co_3O_4 provides a novel potential material for fabricating nonenzymatic electrochemical sensors.

3.3 Reproducibility and Stability

The amperometric responses with six electrodes fabricated from different batches were recorded to evaluate the precision of the proposed strategy. The intra-assay variation coefficient was 3.8%, demonstrating good reproducibility of the Au@C-Co_3O_4 modified GC electrode.

Stability is another important issue for the practical implementation of H_2O_2 detection. There was less than 3% drift in *i–t* curve during the 1000 s measurement (Fig. S11), and this indicated the good operational stability of the sensor. Moreover, the H_2O_2 sensor could retain 90% of the initial amperometric response after storage in 0.1 M PBS (pH 7.4) at 4 °C for two months (Fig. S12), revealing its good storage stability.

3.4 Selectivity Study

To demonstrate the selectivity of Au@C-Co_3O_4 for H_2O_2 detection, several potential interferences in living cells were tested. As exhibited in Fig. S13, Au@C-Co_3O_4/GCE showed obvious amperometric response toward 0.05 mM H_2O_2. With a further injection of 0.1 mM ascorbic acid (AA), uric acid (UA), dopamine (DA), cysteine, glutamic acid, glycine, glutathione, or 1.0 mM inorganic ions (Na^+, K^+, Mg^{2+}, Ca^{2+}, H^+, and Cl^-), there were no noteworthy amperometric responses observed. Co_3O_4-based materials are commonly used to detect glucose; however, no obvious response was found upon the addition of glucose, which had a 10-fold higher concentration than that of H_2O_2, and this highlights the remarkable specificity of Au@C-Co_3O_4/GCE for H_2O_2. The optimal applied voltage of +0.50 V is too small to achieve the oxidation of glucose (Fig. S14), thus greatly reducing the interference of glucose. The superior selectivity can be attributed to the strong catalase-like activity of

Co_3O_4 and the relatively lower pH of the electrolyte (Dong et al., 2014).

3.5 In Vitro Cytotoxicity Examination

To determine cytotoxicity, HKC cells, HeLa cells, and MCF-7 cells were seeded in 96-well plates for 12 h to allow cell attachment. Then, the cells were cultured with Au@C-Co_3O_4 (8 μL, 1.0 mg mL^{-1}) for 24 h. According to the MTT cytotoxicity assays, the living cells showed an excellent cell viability of >90% (Fig. S15), indicating the good biocompatibility of Au@C-Co_3O_4.

3.6 Measurements of H_2O_2 Released from Living Cells

H_2O_2 plays important roles in many biological processes, especially in a cellular environment (Kaçar et al., 2014). After achieving high sensitivity with Au@C-Co_3O_4/GCE, the potential practical application of Au@C-Co_3O_4/GCE was further investigated by detecting H_2O_2 released from living cells. H_2O_2 release was triggered by adding PMA, which can resemble the oxidative metabolism most likely to be encountered in vivo (Chang et al., 2013). In the presence of HKC cells, HeLa cells or MCF-7 cells, the addition of PMA (10 μL, 1 μg mL^{-1}) led to an immediate current response (Fig. 4A). Without cells (or cells pretreated with catalase, which is a selective scavenger of H_2O_2), no current response was recorded, thus suggesting that the current change is due to H_2O_2 being

released from the living cells (Maji et al., 2014). We can further distinguish these cells according to the current response (Fig. 4B). For example, the current change for non-cancerous HKC cells at Au@C-Co_3O_4/GCE is ~0.2 μA, which corresponds to ~0.37 μM (n=3) H_2O_2 released from the cells; however, cancerous HeLa and MCF-7 cells give current changes of 1.1 μA and 1.2 μA, respectively, which correspond to ~2.06 μM and ~2.38 μM H_2O_2 released from these cells. These results are consistent with the tendency of cancerous cells to generate more H_2O_2 because of their fast oxygen metabolism. For comparison, released amounts of H_2O_2 were further evaluated using the reference fluorescence method (Table 1). Relative deviations of the two methods are less than 3%, and this demonstrates the good practicality of the proposed sensor.

Conclusions

In summary, a highly efficient and cost-effective electrocatalyst, porous Au@C-Co_3O_4 hollow dodecahedra was synthesized using a simple strategy that involved the rapid preparation of Au@ZIF-67 template and subsequent two-step thermal annealing of the template at moderate temperature. Benefiting from the unique structural features, the

anisotropic Au@C-Co_3O_4 dodecahedra showed remarkable electrocatalytic performance toward H_2O_2 oxidation, such as good selectivity, ultra-high sensitivity, and quick speed of analysis. These features enable the proposed sensor to be used for real-time monitoring of H_2O_2 released from cells, and this creates a new avenue for developing efficient nonenzymatic electrochemical sensors.

Acknowledgments

The authors are grateful for financial support from the National Natural Science Foundation of China (No. 21675068).

References

Aijaz, A., Masa, J., Rösler, C., Xia, W., Weide, P., Botz, A., Fischer, R., Schuhmann, W., Muhler, M. 2016. Angew. Chem. Inter. Ed. 55, 4087−4091.

Bai, R., Muthoosamy, K., Shipton, F., Pandikumar, A., Rameshkumar, P., Huang, N., Manickam, S. 2016. RSC Adv. 6, 36576−36587.

Bai, R., Muthoosamy, K., Zhou, M., Ashokkumar, M., Huang, N., Manickam, S. 2017. Biosens. Bioelectron. 87, 622−629.

Bajdich, M., García-Mota, M., Vojvodic, A., Nørskov, J., Bell, A. 2013. J.

Am. Chem. Soc. 135, 13521−13530.

Belousov, V., Fradkov, A., Lukyanov, K., Staroverov, D., Shakhbazov, K. S., Terskikh, A., Lukyanov, S. 2006. Nature Methods. 3, 281−286.

Chakraborty, S., Raj, C. 2009. Biosens. Bioelectron. 24, 3264−3268.

Chang, H., Wang, X., Shiu, K., Zhu, Y., Wang, J., Li, Q., Chen, B., Jiang, H. 2013. Biosens. Bioelectron. 41, 789−794

Cheng, C., Zhang, C., Gao, X., Zhuang, Z., Du, C., Chen, W. 2018. Anal. Chem. 90, 1983−1991.

Dai, H., Lü, W., Zuo, X., Zhu, Q., Pan, C., Niu, X., Liu, J., Chen, H., Chen, X. 2017. Biosens. Bioelectron. 95, 131−137.

Dong, J., Song, L., Yin, J., He, W., Wu, Y., Gu, N., Zhang, Y. 2014. ACS App. Mater. Inter. 6, 1959−1970.

Frens, G. 1973. Nat. Phys. Sci. 241, 20−22.

Halliwell, B., Clement, M., Long, L. 2000. FEBS Letters. 486, 10−13.

Heli, H., Pishahang, J. 2014. Electrochim. Acta. 123, 518−526.

Hu, H., Guan, B., Xia, B., Lou, X. 2015. J. Am. Chem. Soc. 137, 5590−5595.

Jiang, J., Li, Y., Liu, J., Huang, X., Yuan, C., Lou, X. 2012. Adv. Mater. 24, 5166–5180.

Kaçar, C., Dalkiran, B., Erden, P., Kiliç, E. 2014. App. Surf. Sci. 311, 139−146.

Kong, D., Luo, J., Wang, Y., Ren, W., Yu, T., Luo, Y., Yang, Y., Cheng, C.

2014. Adv. Funct. Mater. 24, 3815−3826.

Kumar, K., Canaff, C., Rousseau, J., Arrii-Clacens, S., Napporn, T. W., Habrioux, A., Kokoh, K. 2016. J. Phys. Chem. C. 120, 7949−7958.

Li, Z., Xin, Y., Wu, W., Fu, B., Zhang, Z. 2016. Anal. Chem. 88, 7724−7729.

Liu, H., Zhang, S., Liu, Y., Yang, Z., Feng, X., Lu, X., Huo, F. 2015. Small. 11, 3130−3134.

Liu, M., He, S., Chen, W. 2014. Nanoscale. 6, 11769−11776.

Liu, M., Liu, R., Chen, W. 2013. Biosens. Bioelectron. 45, 206−212.

Liu, Y., Liu, X., Guo, Z., Hu, Z., Xue, Z., Lu, X. 2017. Biosens. Bioelectron. 87, 101−107.

Lu, G., Li, S., Guo, Z., Farha, O., Hauser, B., Qi, X., Wang, Y., Wang, X., Han, S., Liu, X., DuChene, J., Zhang, H.; Zhang, Q., Chen, X., Ma, J., Loo, S., Wei, W., Yang, Y., Hupp, J., Huo, F. **2012.** *Nature Chem.* *4*, 310−316.

Ma, T., Dai, S., Jaroniec, M., Qiao, S. 2014. J. Am. Chem. Soc. 136, 13925−13931.

Maji, S., Sreejith, S., Mandal, A., Ma, X., Zhao, Y. 2014. ACS App. Mater. Inter. 6, 13648−13656.

Miller, E., Dickinsion, B., Chang, C. 2010. J. Proc. Natl. Acad. Sci. 7, 15681−15686.

Muthoosamy, K., Manickam, S. 2017. Ultrason. Sonochem. 39, 478−493.

Shi, X., Yao, Y., Xu, Y., Liu, K., Zhu, G., Chi, L., Lu, G. 2017. ACS Appl. Mater. Interfaces. 9, 7481−7488.

Sun, X., Guo, S., Chung, C., Zhu, W., Sun, S. 2013. Adv. Mat. 25, 132−136.

Sun, Y., Luo, M., Meng, X., Xiang, J., Wang, L., Ren, Q., Guo, S. 2017. Anal. Chem. 89, 3761−3767.

Wang, Y., Shao, Y., Matson, D. W., Li, J., Lin, Y. 2010. ACS nano. 4, 1790−1798.

Wu, H., Xia, B., Yu, L., Yu, X., Lou, X. 2015. Nat. Commun. 6, 6512.

Xu, X., Cao, R., Jeong, S., Cho, J. 2012. Nano Lett. 12, 4988−4991.

Yoo, S., Starnes, T., Deng, Q., Huttenlocher, A. 2011. Nature. 480, 109−112.

Yu, X., Yu, L., Wu, H., Lou, X. 2015. Angew. Chem. 127, 5421−5425.

Yang, J., Zhang, F., Lu, H., Hong, X., Jiang, H., Wu, Y., Li, Y. 2015. Angew. Chem. Inter. Ed. 54, 10889−10893.

Zhang, E., Xie, Y., Ci, S., Jia, J., Wen, Z. 2016. Biosens. Bioelectron. 81, 46−53.

Zhang, Y., Bo, X., Nsabimana, A., Luhana, C., Wang, G., Wang, H., Li, M., Guo, L. 2014. Biosens. Bioelectron. 53, 250−256.

Zhang, J., Liu, H., Dou, M., Wang, F., Liu, J., Li, Z., Ji, J. 2015. Electroanal. 27, 1188−1194.

Zhang, L., Wu, H., Lou, X. 2013. J. Am. Chem. Soc. 135, 10664−10672.

Fig. 1. (A) FESEM image of Au@ZIF-67. (B) FESEM image of Au@C-Co_3O_4. (C) EDS pattern of Au@C-Co_3O_4. (D) PXRD pattern of ZIF-67, Au@ZIF-67 and Au@C-Co_3O_4. The insert: (I) TEM image of Au@ZIF-67. (II) TEM image of Au@C-Co_3O_4. (III) SAED pattern of Au@C-Co_3O_4.

Fig. 2. High resolution XPS spectra of Au@C-Co_3O_4: (A) full range, (B) Co 2p, (C) O 1s, (D) C 1s, (E) Au 4f, respectively. (F) EIS of GCE, Au/GCE, C-Co_3O_4/GCE and Au@C-Co_3O_4/GCE. Supporting solution: 5.0 mM $K_3Fe(CN)_6/K_4Fe(CN)_6$ (1:1) containing 0.1 M KCl. The insert: the equivalent circuit used to fit the experimental EIS data.

Fig. 3. CVs of Au/GCE, C-Co_3O_4/GCE and Au@C-Co_3O_4/GCE in the presence (dotted line) and absence (solid line) of 0.05 mM H_2O_2 in different electrolyte: (A) 0.1 M NaOH solution, (B) 0.1 M PBS (pH 7.4). Scan rate: 50 mV s^{-1}. (C) CVs of Au@C-Co_3O_4/GCE recorded in 0.1 M PBS (pH 7.4) at different potential scan rates from 5 to 200 mV s^{-1}. Insert: the dependence of redox peak currents on the potential scan rates. (D) CVs of Au@C-Co_3O_4/GCE in 0.1 M PBS (pH 7.4) with different concentrations of H_2O_2. Scan rate: 50 mV s^{-1}. (E) Typical amperometric current−time curves of Au@C-Co_3O_4/GCE with successive addition of different concentration of H_2O_2 in 0.1 M PBS (pH 7.4) at the potential of +0.50 V. Insert: a partial magnification of the current response toward a low concentration of H_2O_2 solution. (F) The corresponding calibration curve for H_2O_2 sensing.

Fig. 4. (A) Amperometric response of Au@C-Co_3O_4/GCE with the addition of PMA in the presence of living cells with or without addition of 50 μL catalase (300 U mL^{-1}) at +0.50 V. (B) Comparison in cellular assay of H_2O_2 detection for HKC, HeLa, and MCF-7 cells.

Scheme 1. Schematic illustration of the synthesis of porous Au@C-Co_3O_4 and the modified GCE used for detecting H_2O_2 release from cells stimulated with PMA.

Fig. 1.

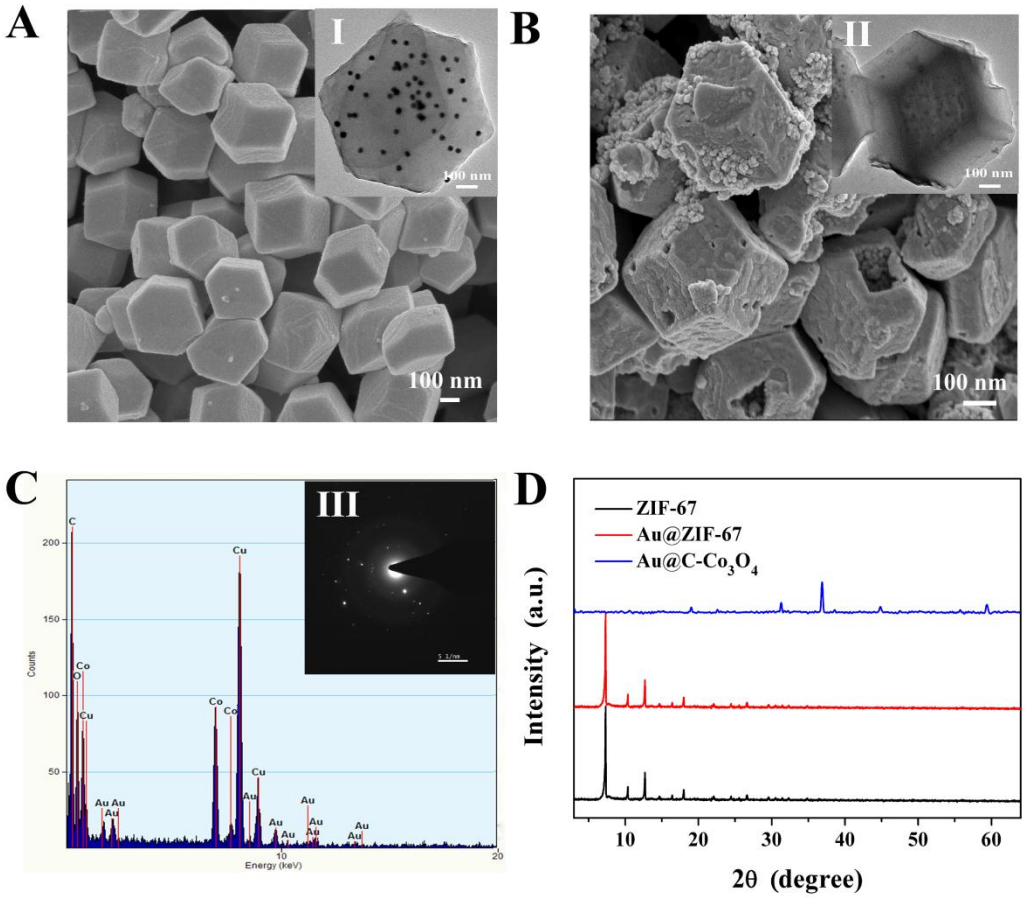

Fig. 2.

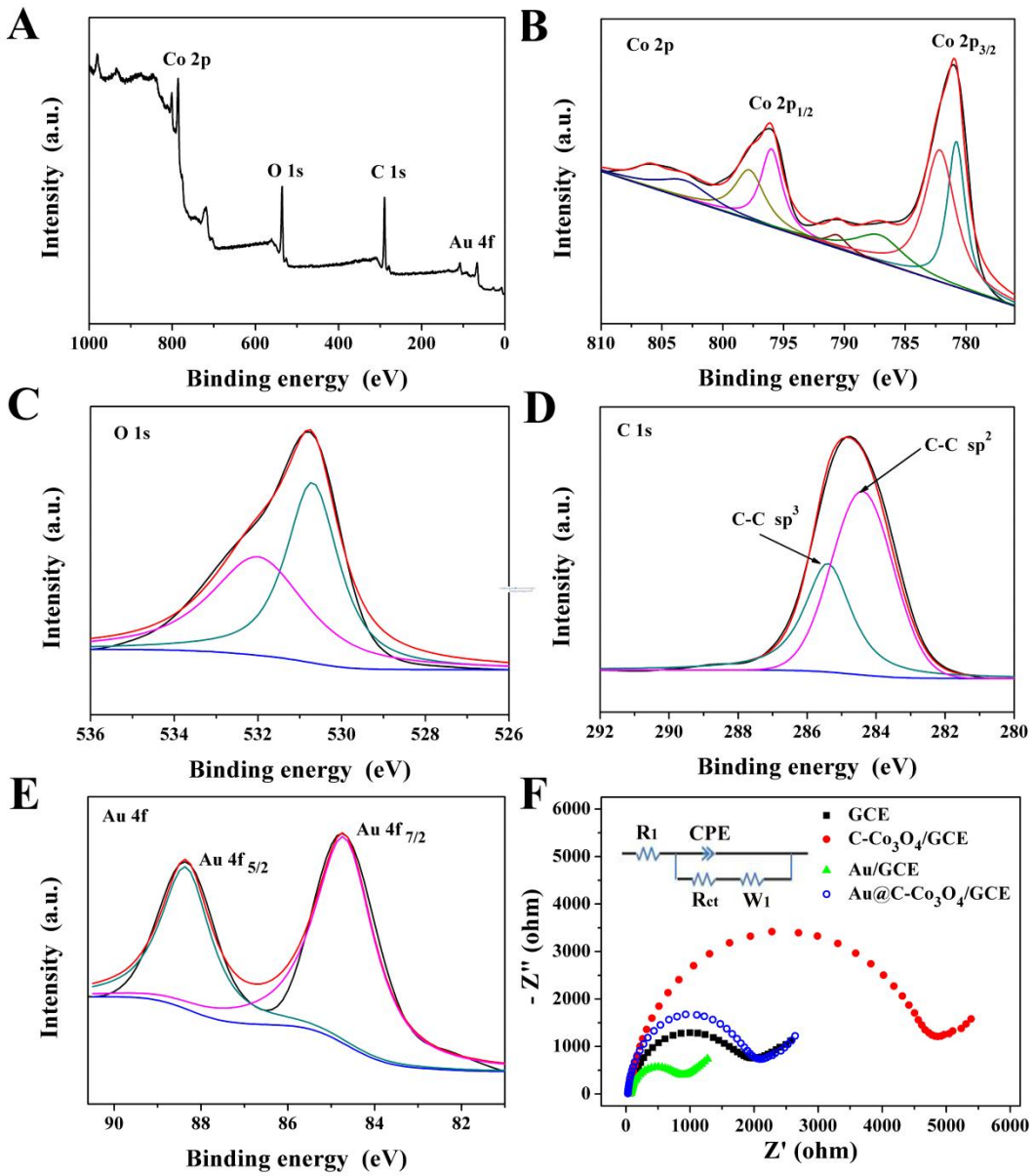
A
Co 2p
O 1s
C 1s
Au 4f
Intensity (a.u.)
Binding energy (eV)
B
Co 2p
Co 2p1/2
Co 2p3/2
C
O 1s
D
C 1s
C-C sp2
C-C sp3
E
Au 4f
Au 4f5/2
Au 4f7/2
F
R1
CPE
Rct
W1
GCE
C-Co3O4/GCE
Au/GCE
Au@C-Co3O4/GCE
- Z'' (ohm)
Z' (ohm)

Fig. 3.

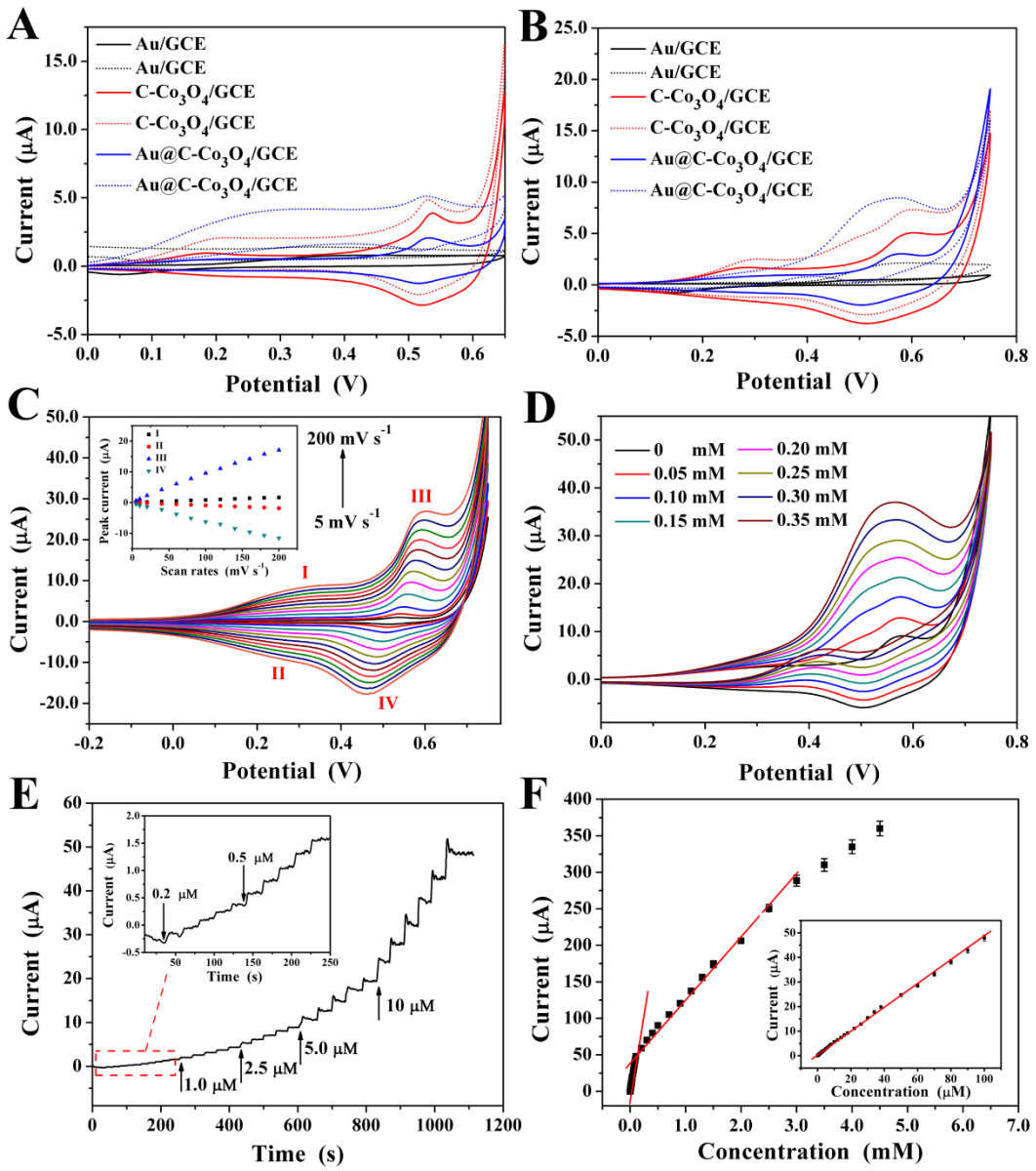
A
Au/GCE
Au/GCE
C-Co3O4/GCE
C-Co3O4/GCE
Au@C-Co3O4/GCE
Au@C-Co3O4/GCE
Current (μA)
Potential (V)
B
Au/GCE
Au/GCE
C-Co3O4/GCE
C-Co3O4/GCE
Au@C-Co3O4/GCE
Au@C-Co3O4/GCE
Current (μA)
Potential (V)
C
200 mV s-1
5 mV s-1
I
II
III
IV
Peak current (μA)
Scan rates (mV s-1)
Current (μA)
Potential (V)
D
0 mM
0.05 mM
0.10 mM
0.15 mM
0.20 mM
0.25 mM
0.30 mM
0.35 mM
Current (μA)
Potential (V)
E
0.2 μM
0.5 μM
1.0 μM
2.5 μM
5.0 μM
10 μM
Current (μA)
Time (s)
F
Current (μA)
Concentration (mM)
Concentration (μM)

Fig. 4.

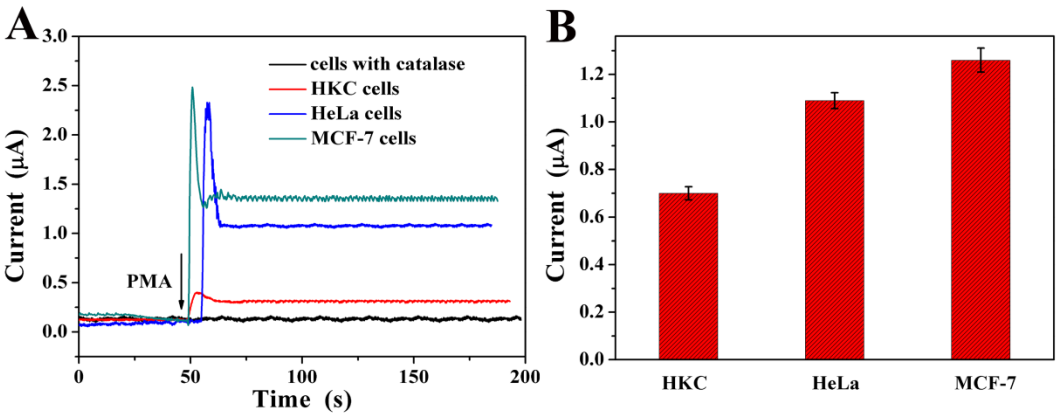

Scheme 1.

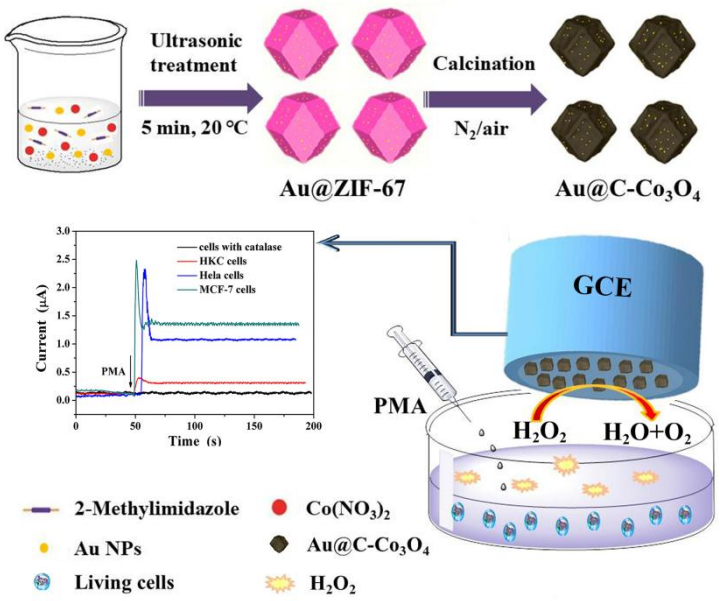

Table 1. Determination of H_2O_2 released from living cells (1×10^6). (*n*=3)

Sample	Proposed biosensor (μM)	Molecular Probes* (μM)	Relative deviation (%)
HKC cells	1.32	1.30	1.54
HeLa cells	2.06	2.10	-1.90
MCF-7 cells	2.38	2.43	-2.06

* Extracellular hydrogen peroxide levels were measured using an Amplex Red Hydrogen Peroxide Assay kit (Molecular Probes) according to the manufacturer's instruction.

Highlights

- Heterogeneous Co_3O_4 dodecahedrons containing carbon and encapsulated Au nanoparticles (Au@C-Co_3O_4) were synthesized by a sacrificial template method.
- The Au@C-Co_3O_4 based electrochemical sensor for H_2O_2 exhibited an ultra-high sensitivity of 7553 μA mM^{-1} cm^{-2} and a low limit of detection of 19 nM.
- The proposed sensor was used to monitor H_2O_2 concentration released from living cells and identify cancer cells.